European Journal of Mechanics / A Solids 111 (2025) 105590

Contents lists available at ScienceDirect

European Journal of Mechanics / A Solids

journal homepage: www.elsevier.com/locate/ejmsol

Full length article

On the inadequacy of a stepped-beam approach in predicting shear stresses in tapered slender solids

Giovanni Migliaccio [a,b,*], Francesco D'Annibale [a,c,1]

[a] Department of Civil, Construction-Architectural and Environmental Engineering (DICEAA), University of L'Aquila, L'Aquila, Italy
[b] National Group for Mathematical Physics (GNFM), L'Aquila, Italy
[c] International Research Center on Mathematics and Mechanics of Complex Systems (M&MoCS), L'Aquila, Italy

ARTICLE INFO

Keywords:
Tapered beam
Stepped beam
Flexure problem
Shear stresses

ABSTRACT

The stress state in slender elastic cylinders with a straight axis and tapered cross-sections is investigated. Compared to the de Saint-Venant's cylinder, the continuous variation in the dimensions of the cross-sections along the cylinder's axis results in additional, non-trivial shear stress distributions within the cross-sections. This paper analytically investigates the dependence of these stresses on taper, a topic of significant practical interest for the design of tapered structural elements commonly employed in various engineering applications, such as components of wind turbines, aircraft, and bridges. The analytical study in this paper is based on a set of partial differential equations and boundary conditions, derived in a recent work, that govern the stress state in three-dimensional tapered cylinders undergoing cross-sectional warping, in- and out-of-plane. A new analytical solution is derived for rectangular cross-sectioned tapered cylinders, resembling the shear webs of large wind turbine blades, with external loads applied at the ends. By examining this paradigmatic case, the inadequacy of approaches based on stepped-beam models in predicting shear stresses in tapered slender solids is demonstrated analytically. Numerical examples, including comparisons to results from the literature and benchmark solutions based on finite element methods, are also provided and corroborate the analytical findings of this study.

1. Introduction

Tapered structural elements are widely employed in civil and industrial engineering applications because they allow optimal compromises to be achieved between structural strength, material usage and cost (Atkin, 1938; Vilar et al., 2021; Bertolini and Taglialegne, 2020; DesRoches et al., 2022; Balduzzi et al., 2017). The advantages of using tapered elements over prismatic ones is known as early as the 17th century. The first systematic study of the mechanical behaviour of slender elements with different shapes, under various loading conditions, dates back to Galileo Galilei. Galileo's work *Discorsi e Dimostrazioni Matematiche intorno a due Nuove Scienze Attinenti alla Mecanica* (Galilei, 1638), published in 1638 and translated in English in 1954 with the title *Two New Sciences* (Galilei, 1954), is structured as a dialogue over four days among three characters: Francesco Sagredo, Filippo Salviati (who represents Galileo) and Simplicio. On the second day of the dialogue, the discussion focuses on the behaviour of a cantilever beam with a prescribed load applied at the free end and on the resistance of such beam if part of its material is removed, i.e., the so-called problem of the *solid of equal resistance* (Galilei, 1638, 1954).

Saving material without compromising the *resistance* of the structure is a common design requirement for engineers. Examples of modern structural elements that adhere to this design requirement include towers and blades of horizontal-axis wind turbines in industrial engineering (Griffith et al., 2012; Migliaccio et al., 2020), tapered components of aircraft wings and tailplanes in the aerospace sector (Atkin, 1938; Pugsley and Weatherhead, 1942), and variable-height beams in bridge construction within the civil engineering field (Paglietti and Carta, 2009; Balduzzi et al., 2016). Accurate predictions of their state of stress and strain is important even in the preliminary design stage. However, critical issues are not absent in engineering methods commonly used by practitioners for analysis and design (Paglietti and Carta, 2009; Balduzzi et al., 2017; Migliaccio et al., 2022), which often rely on approaches based on stepped-beam models.

This paper addresses the analytical prediction of stresses and strains in slender tapered elements, proposes new analytical formulas that can be used for stress analyses, and discusses the effects of taper that make

* Corresponding author.
E-mail addresses: giovanni.migliaccio@univaq.it (G. Migliaccio), francesco.dannibale@univaq.it (F. D'Annibale).
[1] Contributing authors.

https://doi.org/10.1016/j.euromechsol.2025.105590
Received 22 November 2024; Received in revised form 24 January 2025; Accepted 26 January 2025
Available online 3 February 2025

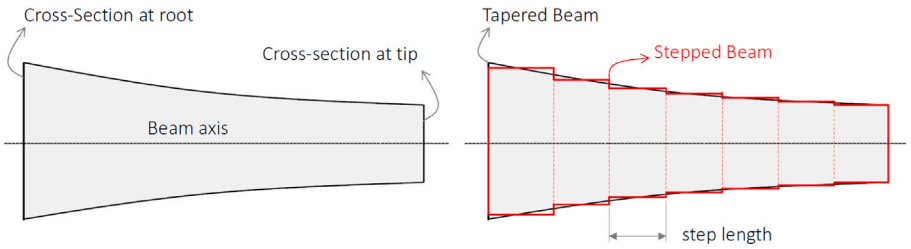

Fig. 1. Lateral view of a tapered beam (left) with indication of the beam's axis and of the end cross-sections; stepped beam (right) that geometrically approximates the tapered beam.

stepped-beam approaches inadequate in predicting stresses and strains in tapered elements.

The structural element addressed in this study has the shape of a slender elastic cylinder with a straight axis and tapered cross-sections and is subjected to external loads applied at its end cross-sections. Compared to the well-known de Saint-Venant's cylinder (Navier, 1864; Sokolnikoff, 1946; Muskhelishvili, 1977), the continuous variation in cross-sectional dimensions along the cylinder's axis generates additional, non-trivial stress distributions within the cross-sections. These stress distributions (it will be shown in this work) cannot be accurately predicted using stepped-beam approaches, challenging the common engineering perception, notwithstanding the fact that the effects of taper on the deflection of the axis of a tapered cylinder can be effectively predicted using such approaches. In stepped-beam models, indeed, the idea is to approximate the shape of the tapered cylinder with a suitable stepped beam containing an adequate number of segments or steps, as illustrated in Fig. 1. Furthermore, by continuously increasing the number of steps in such a beam, the displacement of the points of its axis can be made to closely approximate those of the tapered cylinder, according to a specified convergence criterion. Unfortunately, this approach does not yield the same accuracy for the stresses and strains within the cross-sections, which can be quite different from those obtainable by resorting to stepped-beam approaches (Migliaccio and Ruta, 2020; Migliaccio, 2023a). This is due to stress fields that explicitly depend on the continuous variation in cross-sectional dimensions along the cylinder's axis, which are absent in stepped-beam models but are crucial for accurate stress predictions, as is demonstrated in the present work.

Given the importance of accurately predicting stresses and strains in tapered elements, many researchers have addressed the development of engineering methods and formulas for their analysis and design. Building on de Saint-Venant's findings on stresses and strains in prismatic cylinders (Navier, 1864; Love, 1944; Sokolnikoff, 1946; Muskhelishvili, 1977), and with the aim of generalizing solutions like Jourawski's shear formula (Jourawski, 1856), developed in the mid-19th century for designing bridge beams during the construction of the St. Petersburg-Moscow railroad (1844–1850), several researchers have attempted to derive similar solutions and formulas for tapered elements. Among them, it is noteworthy the early work of Bleich (1932) for bridge engineering applications, the studies of Atkin (1938), Saksena (1944), and Krahula (1975) on tapered structural elements used in the aerospace sector, the survey of Paglietti and Carta (2009) on the theory of shear strength for variable-depth beams, the works of Balduzzi et al. (2016, 2017), Mercuri et al. (2020) on the deficiencies in modern engineering tools and procedures for the analysis of tapered thin-walled beams, the investigations of Bertolini et al. (2019a,b), Bertolini and Taglialegne (2020), Bennati et al. (2016) and Migliaccio and Ruta (2020), Migliaccio (2022a,b), Migliaccio and Ruta (2021), Migliaccio (2023b) on stresses and strains in tapered components of large horizontal axis wind turbines, and other works (Vilar et al., 2021; Slocum, 1911; Xu and Zhou, 2009; Trahair and Ansourian, 2016; Shin et al., 2016; Zappino et al., 2018; Chockalingam et al., 2020; Su and Zhou, 2022) recalled in recent papers (Paglietti and Carta, 2009; Balduzzi et al., 2017; Migliaccio et al., 2022), where further references can be found.

The study of tapered elements for structural engineering applications continues nowadays to attract the interest of many researchers. Analytical solutions have been proposed by some authors for thin, tapered elements under plane stress conditions (Atkin, 1938; Hodges et al., 2008, 2010; Trahair and Ansourian, 2016), often drawing parallels to the planar wedge problem outlined in classical elasticity treatises, such as Timoshenko and Goodier (1951). Other authors have concentrated on thin-walled tapered beams (Balduzzi et al., 2016; Bertolini et al., 2019a; Vilar et al., 2021), assuming Navier's formula (Navier, 1864) to hold for the cross-sectional normal stresses and deriving the relevant shear stresses via the static equilibrium of the beam in its undeformed configuration, following Jourawksi's method (Jourawski, 1856). Yet others have addressed the problem of stress prediction in tapered elements via numerical methods (Shin et al., 2016; Zappino et al., 2018; Patni et al., 2020; Sarhadi and Eder, 2024; Vo et al., 2021). Numerical approaches are flexible and well-suited for detailed, accurate analyses. On the other hand, analytical solutions offer insights into the physical problem that are often inaccessible through purely numerical investigations.

The present work adopts an analytical approach proposed in a recent study for predicting stresses and strains in tapered cylinders (see, e.g., Migliaccio and Ruta (2021), Migliaccio (2023a)). These cylinders are treated as slender, three-dimensional elastic solids with cross-sections capable of both in-plane and out-of-plane deformation. The analytical approach relies on a variational principle to derive the governing equations for the stress state in such elements. These equations are expressed as Partial Differential Equations (PDEs) with suitable boundary conditions, similar to the PDEs governing the stress state in the de Saint-Venant's cylinder. PDEs problems generally admit closed-form analytical solutions only in few cases, as also discussed in Migliaccio and Ruta (2021), Migliaccio (2022b), where tapered cylinders with elliptical pre-twisted cross-sections are solved analytically and the solutions are validated by comparisons with the results of finite element methods. The PDEs problems reported in Migliaccio and Ruta (2021), Migliaccio (2023a) are recalled in this paper and a new analytical solution is found for a rectangular cross-sectioned tapered cylinder with external actions applied only at the end cross-sections. The new analytical expressions of stresses and strains derived in this work represent a generalization of those that are valid for the de Saint-Venant's cylinder and recover them in the prismatic case. Furthermore, they demonstrate analytically the inadequacy of approaches based on stepped-beam models when dealing with stress predictions in tapered slender solids.

The paper is organized as follows. The mechanical model and the relevant partial differential equations that govern the stress state in the considered elastic solid are recalled in Section 2. A new analytical solution to such PDEs for the case of a rectangular cross-sectioned tapered cylinder is presented in Section 3 and complemented with additional details in Appendix. This solution is applied in Section 4 to structural elements of interest from both theoretical and practical engineering perspectives, highlighting the inadequacy of approaches based on stepped-beam models in predicting shear stresses in tapered elements. Numerical examples, reported in Section 5, confirm the analytical findings of the study. Conclusions and possible future works are illustrated in Section 6.

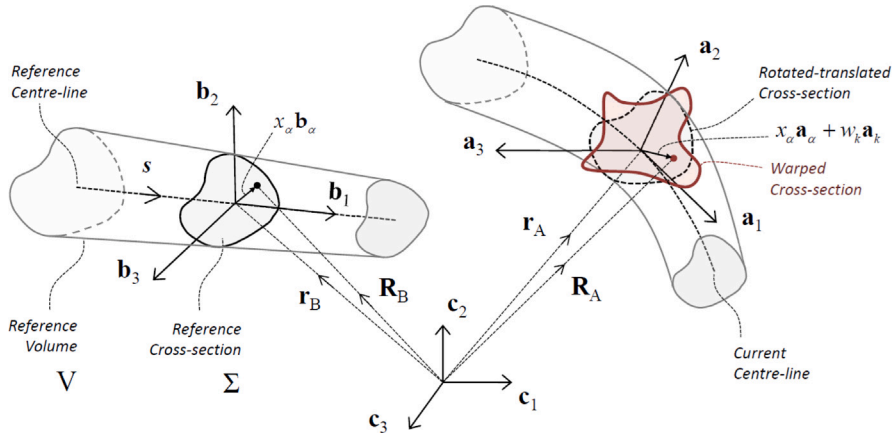

Fig. 2. Schematic of tapered slender solid in its reference undeformed (left) and current deformed (right) states, with indication of the corresponding centre-lines, cross-sections, and local coordinate systems, $\mathbf{b}_i$ and $\mathbf{a}_i$, $i = 1,2,3$: the axial coordinate s and cross-sectional coordinates x_α, $\alpha = 2,3$, in the reference state define the position of the cylinder's points; the warping fields w_i in the current state are the in- and out-of-plane displacements of the cross-sections.

2. Mechanical model

This section recalls the tapered cylinder model introduced in recent works (e.g., Migliaccio and Ruta (2021), Migliaccio et al. (2022), Migliaccio (2023a)), to which readers can refer for further details. The main definitions concerning the tapered geometry, as well as the stress and strain measures adopted in the present work, are presented in Section 2.1. Section 2.2 subsequently describes the partial differential equations (PDEs) and boundary conditions relevant to this study, which are analytically solved in Section 3.

2.1. Preliminary definitions

A schematic depiction of the considered cylinder, in both its reference *undeformed* and current *deformed* states, is presented in Fig. 2. This cylinder is schematized as a series of deformable plane figures (cross-sections) attached at a deformable line (axis or centre-line), occupying a region of volume V in the reference state. It is assumed that in the reference state the cylinder's cross-sections are orthogonal to the centre-line at the centroid and the centre-line is a straight regular curve. The centre-line may undergo small displacements and strains. The cross-sections follow the centre-line motion and may undergo additional small warping displacements, in and out of plane, producing small deformation of the cross-sections.

Two local coordinate systems are introduced in Fig. 2. The first, with orthogonal unit vectors $\mathbf{b}_i$, $i = 1,2,3$, is defined at any point along the centre-line in the reference state and depends on the arc-length s, i.e., $\mathbf{b}_i = \mathbf{b}_i(s)$, with $\mathbf{b}_1$ tangent to the reference centre-line, $\mathbf{b}_2$ and $\mathbf{b}_3$ contained in the cross-sectional plane. The second, with orthogonal unit vectors $\mathbf{a}_i$, $i = 1,2,3$, is defined at any point along the centre-line in the current state and depends on the arc-length s and time t, i.e., $\mathbf{a}_i = \mathbf{a}_i(s,t)$, with $\mathbf{a}_1$ tangent to the deformed centre-line. Unlike the reference state, in which a cross-section, Σ, is contained in the plane of $\mathbf{b}_2$ and $\mathbf{b}_3$, in the current state a cross-section may not remain plane and may not belong to the plane of $\mathbf{a}_2$ and $\mathbf{a}_3$.

For convenience, a fixed Cartesian reference frame is also introduced. The corresponding orthogonal unit vectors are $\mathbf{c}_i$, $i = 1,2,3$. The orientation of the unit vectors $\mathbf{a}_i$ and $\mathbf{b}_i$ relative to the unit vectors $\mathbf{c}_i$ can be defined in terms of two proper orthogonal tensor fields $\mathbf{A} = \mathbf{a}_i \otimes \mathbf{c}_i$ and $\mathbf{B} = \mathbf{b}_i \otimes \mathbf{c}_i$, at any point along the centre-line ($s \in [0, L]$), where $\otimes$ is the usual tensor or dyadic product. Similarly, the orientation of the unit vectors $\mathbf{a}_i$ relative to the unit vectors $\mathbf{b}_i$ can be defined through the proper orthogonal tensor field $\mathbf{T} = \mathbf{a}_i \otimes \mathbf{b}_i = \mathbf{A}\mathbf{B}^T$. Here and throughout the paper standard summation convention is adopted for indexed variables: Latin (Greek) indices takes values 1, 2, 3 (2, 3); repeated indices are summed over their range.

The formal expressions describing the position of the cylinder's points in the reference state, $\mathbf{R}_B$, and in the current state, $\mathbf{R}_A$, are

$$\mathbf{R}_B(z_i) = \mathbf{r}_B(z_1) + x_\alpha(z_i)\mathbf{b}_\alpha(z_1)\,, \tag{1a}$$

$$\mathbf{R}_A(z_i,t) = \mathbf{r}_A(z_1,t) + x_\alpha(z_i)\mathbf{a}_\alpha(z_1,t) + w_k(z_i,t)\mathbf{a}_k(z_1,t)\,, \tag{1b}$$

where $\mathbf{r}_B$ and $\mathbf{r}_A$ denote the position of the centre-lines in the reference and current states, respectively, x_α identify the points in the cross-sections, w_i are warping displacements introduced to model the in- and out-of-plane deformation of the cross-sections, and, finally, z_i are time-independent mathematical variables spanning a prismatic three-dimensional domain that is mapped into the tapered domain occupied by the cylinder through the relations $x_1 = z_1 = s$, $x_2 = \Lambda_2(s)z_2$ and $x_3 = \Lambda_3(s)z_3$, where $\Lambda_2(s)$ and $\Lambda_3(s)$ are prescribed taper functions. Henceforth, and throughout the paper, the dependence of all scalar, vector, and tensor fields on the spatial variables z_i or x_i and on the time t is understood and, hence, omitted.

The state of strain in the cylinder is described by the Green–Lagrange strain tensor field $\mathbf{E}$ and by the vector fields $\boldsymbol{\gamma} = \mathbf{T}^T\mathbf{r}_A' - \mathbf{r}_B'$ and $\mathbf{k} = \mathbf{T}^T\mathbf{k}_A' - \mathbf{k}_B'$, as in Migliaccio and Ruta (2020), Migliaccio et al. (2020), where prime stands for s-derivative. It is noted that in the present work the curvature vector $\mathbf{k}_B$ vanishes identically ($\mathbf{k}_B = 0$) because the reference centre-line is a straight regular curve and the reference cross-sections are not pre-twisted. The curvature vector $\mathbf{k}_A$ coincides with the axial vector of the skew tensor $\mathbf{K}_A = \mathbf{A}'\mathbf{A}^T$.

The vector fields $\mathbf{k} = k_i\mathbf{b}_i$ and $\boldsymbol{\gamma} = \gamma_i\mathbf{b}_i$ are referred to as one-dimensional strain measures because they only capture variations in the curvature vector and in the centre-line tangent between the reference and current states. In contrast, the tensor field $\mathbf{E} = E_{ij}\mathbf{b}_i \otimes \mathbf{b}_j$ is a three-dimensional strain measure that also accounts for the deformation of the cylinder's cross-sections, and is defined by the usual relation

$$\mathbf{E} = \frac{\mathbf{H}^T\mathbf{H} - \mathbf{I}}{2}\,, \tag{2}$$

where $\mathbf{I}$ denotes the identity tensor, and $\mathbf{H}$ is the deformation gradient, i.e., the derivative of $\mathbf{R}_A$ with respect to $\mathbf{R}_B$,

$$\mathbf{H} = \frac{\partial \mathbf{R}_A}{\partial \mathbf{R}_B}\,. \tag{3}$$

The state of stress in the cylinder is described through the second (symmetric) Piola–Kirchhoff stress tensor, $\mathbf{S} = S_{ij}\mathbf{b}_i \otimes \mathbf{b}_j$. Considering a linear, elastic, isotropic, and homogeneous material (Gurtin, 1981), the components S_{ij} of the stress tensor $\mathbf{S}$ are expressed in terms of the components E_{ij} of the Green–Lagrange strain tensor $\mathbf{E}$,

$$S_{ij} = \frac{Y}{1+\nu}E_{ij} + \frac{\nu Y}{(1+\nu)(1-2\nu)}E_{kk}\delta_{ij}\,, \tag{4}$$

where δ_{ij} is the Kronecker's delta ($\delta_{ij} = 1$ when $i = j$, 0 otherwise), Y is the Young's modulus of the material, and ν is the Poisson's ratio. For completeness, the shear modulus of the material, G, is also introduced: it is related to Young's modulus and Poisson's ratio by the usual relation $2G = Y/(1+\nu)$.

The stress and strain fields introduced so far can be obtained as solution to a set of partial differential equations (PDEs) and boundary conditions (BCs) derivable through the principle of virtual power (Rubin, 2000; Dell'Isola and Bichara, 2005; Ruta et al., 2006). To exploit this principle, two functionals are defined, namely, the external power functional $\mathbf{\Pi}_e$ and the internal power functional $\mathbf{\Pi}_i$. The former, $\mathbf{\Pi}_e$, describes, for each velocity field attainable by the body, interactions between the body and the external environment. Such interactions may take place via contact and non-contact actions. Specifically, it is assumed

$$\mathbf{\Pi}_e = \int_V \mathbf{f}\cdot\mathbf{v} + \int_{\partial V} \mathbf{p}\cdot\mathbf{v}\,, \tag{5}$$

where dot denotes the usual scalar product, vector $\mathbf{f}$ represents body loads (non-contact actions) per unit body's reference volume V, vector $\mathbf{p}$ stands for surface loads (contact actions) per unit area of the body's boundary ∂V, and, finally, vector $\mathbf{v}$ is the time rate of the current position of the body's points. It is noted that the integrals are performed, respectively, over the body's reference volume V, also represented in Fig. 2 (left), and its boundary ∂V. Interactions among the body's parts are described via the internal power functional $\mathbf{\Pi}_i$, that is,

$$\mathbf{\Pi}_i = \frac{d}{dt}\int_V \mathit{\Phi}\,, \tag{6}$$

where $\mathit{\Phi} = \mathbf{S}\cdot\mathbf{E}/2$ is the body strain energy density. Balance equations are finally obtainable via the classical principle of virtual power (Rubin, 2000; Dell'Isola and Bichara, 2005; dell'Isola et al., 2022; Ruta et al., 2006), by requiring that for any velocity field attainable by the body its interactions with the external environment and among its parts are such that the total power vanishes (i.e., $\mathbf{\Pi}_e = \mathbf{\Pi}_i$) at any value of the evolution parameter t. This yields the set of partial differential equations and boundary conditions reported in recent works (Migliaccio and Ruta, 2021; Migliaccio et al., 2022; Migliaccio, 2023a), which govern the stress state of the elastic cylinder under consideration. Those that are relevant to the present study are reported in the next Section 2.2.

2.2. Shear stresses and related PDEs problem

We are now in a position to write the expressions of the stress fields S_{21} and S_{31}, namely, the two components of the second (symmetric) Piola–Kirchhoff stress tensor, $\mathbf{S} = S_{ij}\mathbf{b}_i\otimes\mathbf{b}_j$, that are relevant to the present investigation. Following (Migliaccio and Ruta, 2021; Migliaccio, 2023a), the shear stresses S_{21} and S_{31}, in the considered tapered cylinder, subjected to external actions applied solely at the end cross-sections, are given by

$$S_{21} = G\varphi_2 + G\left(\frac{\partial\omega}{\partial x_2} - k_1 x_3\right) + Y(\gamma_1 + k_2 x_3 - k_3 x_2)\frac{\Lambda_2'}{\Lambda_2}x_2\,, \tag{7a}$$

$$S_{31} = G\varphi_3 + G\left(\frac{\partial\omega}{\partial x_3} + k_1 x_2\right) + Y(\gamma_1 + k_2 x_3 - k_3 x_2)\frac{\Lambda_3'}{\Lambda_3}x_3\,, \tag{7b}$$

where Y and G are the Young's and shear moduli, x_2 and x_3 are spatial variables specifying the position of points within the cylinder's cross-sections, γ_1 represents the extension of the cylinder's centre-line, k_1 and k_α ($\alpha = 2, 3$) are torsional and bending curvatures, respectively, and, finally, the scalar fields ω, φ_2, and φ_3 (depending on the cross-sectional variables x_2 and x_3) must satisfy partial differential equations,

$$\frac{\partial^2\omega}{\partial x_2^2} + \frac{\partial^2\omega}{\partial x_3^2} = 0\,, \tag{8a}$$

$$\frac{\partial\varphi_2}{\partial x_2} + \frac{\partial\varphi_3}{\partial x_3} = p_2 x_2 + p_3 x_3\,, \tag{8b}$$

$$\frac{\partial\varphi_3}{\partial x_2} - \frac{\partial\varphi_2}{\partial x_3} = q_2 x_2 + q_3 x_3\,, \tag{8c}$$

with Neumann-type boundary conditions on the boundary $\partial\Sigma$ of the cross-sectional domain Σ,

$$\left(\frac{\partial\omega}{\partial x_2} - k_1 x_3\right)n_2 + \left(\frac{\partial\omega}{\partial x_3} + k_1 x_2\right)n_3 = 0\,, \tag{9a}$$

$$\varphi_2 n_2 + \varphi_3 n_3 = 0\,. \tag{9b}$$

In Eqs. (8)–(9), n_α are the components of the outward unit normal on $\partial\Sigma$, and coefficients p_2, p_3, q_2, and q_3 are defined as follows

$$p_2 = 2(1+\nu)k_3' + 2(1+\nu)\left(\frac{\Lambda_3'}{\Lambda_3} + 2\frac{\Lambda_2'}{\Lambda_2}\right)k_3\,, \tag{10a}$$

$$p_3 = -2(1+\nu)k_2' - 2(1+\nu)\left(\frac{\Lambda_2'}{\Lambda_2} + 2\frac{\Lambda_3'}{\Lambda_3}\right)k_2\,, \tag{10b}$$

$$q_2 = 2\nu k_2' + 2(1+\nu)\frac{\Lambda_2'}{\Lambda_2}k_2\,, \tag{10c}$$

$$q_3 = 2\nu k_3' + 2(1+\nu)\frac{\Lambda_3'}{\Lambda_3}k_3\,, \tag{10d}$$

where ν is the material Poisson's ratio, $\Lambda_2(s)$ and $\Lambda_3(s)$ are taper functions, which define the law of variation of the cross-sectional dimensions of the cylinder along the cross-sectional axes x_2 and x_3, respectively, and a prime (as in Λ_2') stands for derivative with respect to the axial variable s, namely, the arc-length of the cylinder's centre-line in the reference configuration (Fig. 2).

Eqs. (7)–(10) show the role of the scalar fields ω, φ_2 and φ_3 in determining the shear stresses S_{21} and S_{31}. The first scalar field, ω, plays the role of the de Saint-Venant's out-of-plane warping function and is proportional to it through the torsional curvature k_1. The other two, φ_2 and φ_3, are associated with shear strains in the cylinder's cross-sections caused by flexure. It is worth to notice that for a prismatic cylinder in the absence of torsion the classical relations $\varphi_2 = 2E_{21} = S_{21}/G$ and $\varphi_3 = 2E_{31} = S_{31}/G$ are obtained from Eq. (7), where E_{21} and E_{31} are two components of the Green–Lagrange strain tensor, $\mathbf{E} = E_{ij}\mathbf{b}_i\otimes\mathbf{b}_j$.

Other equations (see, e.g., Migliaccio (2023a,b), Migliaccio and Ruta (2021)) govern the determination of the remaining components of the stress and strain tensors, $\mathbf{S}$ and $\mathbf{E}$. However, since this study focuses solely on the effects of taper on the shear stresses $S_{\alpha 1}$ and shear strains $E_{\alpha 1}$ ($\alpha = 2, 3$), the additional equations for the other components of tensors $\mathbf{S}$ and $\mathbf{E}$ are not directly relevant and are therefore omitted from this discussion.

The determination of the shear stresses S_{21} and S_{31} is straightforward once the PDEs problem (8)–(10) has been solved. It is noted that the PDE (8a) with boundary condition (9a) defines an independent PDE problem in terms of ω, whose solution depends solely on the shape of the cross-sectional domain Σ and on the torsional curvature k_1. Similarly, the PDEs (8b)–(8c) with boundary condition (9b) is a PDEs problem in the scalar fields φ_2 and φ_3, whose solution depends only on the shape of the domain Σ, on the bending curvatures k_α and on their s-derivative, k_α'. Such PDE problems formally resemble those that govern the flexural–torsional deformation of the de Saint-Venant's cylinder (Sokolnikoff, 1946; Muskhelishvili, 1977), except for the expressions of coefficients a_α and b_α, which in the present work account for the effects of taper and reduce to those of the de Saint-Venant's cylinder only in the prismatic case ($\Lambda_\alpha = 1$, $\Lambda_\alpha' = 0$). Given this, it is not surprising that the PDEs problem (8)–(10) admits analytical solutions only in a few cases. One such case is presented in the following section.

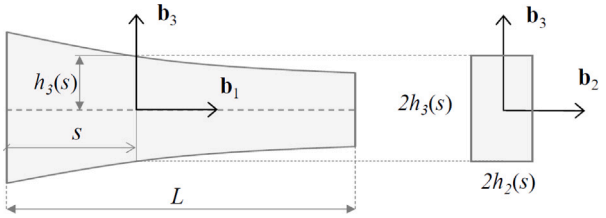

Fig. 3. Reference (underformed) configuration of a tapered cylinder with rectangular solid cross-sections: lateral view (left) and frontal view (right) with indication of the dimensions $h_2(s)$ and $h_3(s)$ of a generic cross-section at the axial coordinate $s \in [0, L]$.

3. A closed-form solution of a paradigmatic case

Let us consider the slender elastic element whose reference undeformed configuration is represented in Fig. 3: it is a rectangular cross-sectioned tapered cylinder, whose cross-sectional dimensions, $2h_2(s)$ and $2h_3(s)$, change between the end cross-sections ($s = 0$ and $s = L$) according to prescribed taper functions, $\Lambda_2(s)$ and $\Lambda_3(s)$, such that $h_2(s) = \Lambda_2(s)H_2$ and $h_3(s) = \Lambda_3(s)H_3$, where $2H_2$ and $2H_3$ are the cross-sectional dimensions at the axial coordinate $s = 0$ (root section). The external actions are applied only at the end cross-sections and are statically equivalent to prescribed forces and moments, as in the de Saint-Venant's cylinder (Sokolnikoff, 1946; Love, 1944; Muskhelishvili, 1977).

For the case at hand, the PDE problem defined by Eqs. (8)–(10) admits an analytical solution, enabling the determination of the shear stresses S_{21} and S_{31}, via Eq. (7), and the corresponding shear strains E_{21} and E_{31}, through the constitutive model (Eq. (4)).

It is noted that, for a given cross-sectional domain Σ, the solution to the PDE problem defined by Eqs. (8a), (9a), which is formally identical to the de Saint-Venant's torsion problem (Sokolnikoff, 1946), depends solely on the torsional curvature k_1. This problem can be solved analytically for a tapered cylinder with rectangular cross-sections. Furthermore, its solution, provided in Appendix, is formally identical to the solution for a de Saint-Venant's cylinder with rectangular cross-sections under pure torsion. Notably, the shear stresses provided by such solution do not explicitly depend on Λ_2' and Λ_3'. The same cannot be said for the PDEs problem defined by Eqs. (8b), (8c), (9b), which formally resembles the de Saint-Venant's flexure problem (Sokolnikoff, 1946). The solution to this latter (reported in Section 3.1) depends on the bending curvatures k_α and their s-derivative k_α' through coefficients a_α and b_α (Eq. (10)), which include terms proportional to coefficients Λ_2' and Λ_3'. These terms produce additional, non trivial shear stress distributions within the cylinder's cross-sections, which vanish identically only for the de Saint-Venant's cylinder. These shear stress distributions (proportional to Λ_2' and Λ_3') can be determined analytically for a tapered cylinder with rectangular cross-sections, as is shown in Section 3.1.

3.1. Shear stresses in the flexure problem

The search for a solution to the PDEs (8b)–(8c) with boundary condition given by Eq. (9b) can be traced back to the search for a harmonic function Ψ, depending on the cross-sectional variables x_2 and x_3, that satisfies the following Neumann-type condition on the boundary $\partial\Sigma$ of the cross-sectional domain Σ:

$$\frac{\partial \Psi}{\partial n} = -\frac{p_2 x_2^2 - q_3 x_3^2}{2} n_2 - \frac{q_2 x_2^2 + p_3 x_3^2}{2} n_3 , \tag{11}$$

where Σ is the rectangle $(x_2, x_3) \in [-h_2, h_2] \times [-h_3, h_3]$. Given the harmonic function Ψ, the scalar fields φ_2 and φ_3 can be determined as follows:

$$\begin{aligned} \varphi_2 &= \frac{p_2 x_2^2 - q_3 x_3^2}{2} + \frac{\partial \Psi}{\partial x_2}, \\ \varphi_3 &= \frac{q_2 x_2^2 + p_3 x_3^2}{2} + \frac{\partial \Psi}{\partial x_3}. \end{aligned} \tag{12}$$

For the problem at hand, the harmonic function Ψ can be represented as a series involving trigonometric and hyperbolic functions:

$$\begin{aligned} \Psi = A_0 x_2 + B_0 x_3 &+ \sum_{n=1}^{\infty} A_n \sinh\left(\frac{n\pi x_2}{h_3}\right) \cos\left(\frac{n\pi x_3}{h_3}\right) \\ &+ \sum_{n=1}^{\infty} B_n \sinh\left(\frac{n\pi x_3}{h_2}\right) \cos\left(\frac{n\pi x_2}{h_2}\right), \end{aligned} \tag{13}$$

where the coefficients A_0, B_0, A_n and B_n are determined by enforcing the boundary condition (11), yielding:

$$\begin{aligned} A_0 &= -\frac{p_2}{2} h_2^2 + \frac{q_3}{2}\frac{h_3^2}{3}, \quad A_n = \frac{2q_3 h_3^3}{\pi^3} \frac{(-1)^n}{\cosh\left(\frac{n\pi h_2}{h_3}\right)}, \\ B_0 &= -\frac{p_3}{2} h_3^2 - \frac{q_2}{2}\frac{h_2^2}{3}, \quad B_n = \frac{2q_2 h_2^3}{\pi^3} \frac{(-1)^n}{\cosh\left(\frac{n\pi h_3}{h_2}\right)}. \end{aligned} \tag{14}$$

By combining Eqs. (7), (10), (12)–(14), analytical expressions are obtained for the shear stresses S_{21} and S_{31} associated with the flexure of the rectangular cross-sectioned tapered cylinder considered in this section. In order to highlight the effect of taper on S_{21} and S_{31}, they are recast in the form:

$$S_{21} = S_{21}^{(1)} + \frac{\Lambda_2'}{\Lambda_2} S_{21}^{(2)} + \frac{\Lambda_3'}{\Lambda_3} S_{21}^{(3)}, \tag{15a}$$

$$S_{31} = S_{31}^{(1)} + \frac{\Lambda_2'}{\Lambda_2} S_{31}^{(2)} + \frac{\Lambda_3'}{\Lambda_3} S_{31}^{(3)}, \tag{15b}$$

with:

$$S_{21}^{(1)} = \frac{F_2}{J_3}\left(\frac{h_2^2 - x_2^2}{2} + \frac{\nu}{1+\nu}\frac{h_3^2 - 3x_3^2}{6} + \frac{2h_3^2\nu}{\pi^2(1+\nu)} f_3\right) - \frac{F_3}{J_2}\frac{2h_2^2\nu}{\pi^2(1+\nu)} f_2, \tag{16a}$$

$$S_{31}^{(1)} = \frac{F_3}{J_2}\left(\frac{h_3^2 - x_3^2}{2} + \frac{\nu}{1+\nu}\frac{h_2^2 - 3x_2^2}{6} + \frac{2h_2^2\nu}{\pi^2(1+\nu)} g_2\right) - \frac{F_2}{J_3}\frac{2h_3^2\nu}{\pi^2(1+\nu)} g_3, \tag{16b}$$

$$\begin{aligned} S_{21}^{(2)} = \frac{F_1}{A} x_2 + \frac{M_2}{J_2}\left(x_2 x_3 - \frac{2h_2^2}{\pi^2(1+\nu)} f_2\right) + \\ \frac{M_3}{J_3}\left(\frac{h_2^2 - 3x_2^2}{2} + \frac{\nu}{1+\nu}\frac{h_3^2 - 3x_3^2}{2} + \frac{6h_3^2\nu}{\pi^2(1+\nu)} f_3\right), \end{aligned} \tag{16c}$$

$$S_{31}^{(2)} = \frac{M_2}{J_2}\left(\frac{h_2^2 - 3x_2^2}{6(1+\nu)} + \frac{2h_2^2}{\pi^2(1+\nu)} g_2\right) - \frac{M_3}{J_3}\frac{6h_3^2\nu}{\pi^2(1+\nu)} g_3, \tag{16d}$$

$$S_{21}^{(3)} = \frac{M_3}{J_3}\left(\frac{3x_3^2 - h_3^2}{6(1+\nu)} - \frac{2h_3^2}{\pi^2(1+\nu)} f_3\right) + \frac{M_2}{J_2}\frac{6h_2^2\nu}{\pi^2(1+\nu)} f_2, \tag{16e}$$

$$\begin{aligned} S_{31}^{(3)} = \frac{F_1}{A} x_3 - \frac{M_3}{J_3}\left(x_2 x_3 - \frac{2h_3^2}{\pi^2(1+\nu)} g_3\right) + \\ \frac{M_2}{J_2}\left(\frac{3x_3^2 - h_3^2}{2} + \frac{\nu}{1+\nu}\frac{3x_2^2 - h_2^2}{2} + \frac{6h_2^2\nu}{\pi^2(1+\nu)} g_2\right), \end{aligned} \tag{16f}$$

where F_i and M_i represent the components of the internal force and moment acting on the cross-section at the axial coordinate s, with respect to the local coordinate system $\mathbf{a}_i$ ($i = 1, 2, 3$), $A = 4h_2h_3$ is the area of the cross-section, $J_2 = 4h_3^3h_2/3$ and $J_3 = 4h_2^3h_3/3$ are the principal moments of inertia of the cross-section, and, finally, functions

f_2, f_3, g_2 and g_3 are defined as follows:

$$
\begin{aligned}
f_2 &= \sum_{n=1}^{\infty} \frac{(-1)^n}{n^2} \frac{\sinh\left(\frac{n\pi x_3}{h_2}\right)}{\cosh\left(\frac{n\pi h_3}{h_2}\right)} \sin\left(\frac{n\pi x_2}{h_2}\right),\\
f_3 &= \sum_{n=1}^{\infty} \frac{(-1)^n}{n^2} \frac{\cosh\left(\frac{n\pi x_2}{h_3}\right)}{\cosh\left(\frac{n\pi h_2}{h_3}\right)} \cos\left(\frac{n\pi x_3}{h_3}\right),\\
g_2 &= \sum_{n=1}^{\infty} \frac{(-1)^n}{n^2} \frac{\cosh\left(\frac{n\pi x_3}{h_2}\right)}{\cosh\left(\frac{n\pi h_3}{h_2}\right)} \cos\left(\frac{n\pi x_2}{h_2}\right),\\
g_3 &= \sum_{n=1}^{\infty} \frac{(-1)^n}{n^2} \frac{\sinh\left(\frac{n\pi x_2}{h_3}\right)}{\cosh\left(\frac{n\pi h_2}{h_3}\right)} \sin\left(\frac{n\pi x_3}{h_3}\right).
\end{aligned}
\tag{17}
$$

Eq. (15) provide the shear stresses $S_{1\alpha}$ ($\alpha = 2, 3$) in the cylinder's cross-sections as the sum of three contributions: the first one, $S_{1\alpha}^{(1)}$, formally coincides with the solution valid for the de Saint-Venant's cylinder (Sokolnikoff, 1946), except for the fact that the dimensions $h_2(s) = \Lambda_2(s)H_2$ and $h_3(s) = \Lambda_3(s)H_3$ of the cross-sections are not constant in the present case (they vary along the cylinder's axis according to general taper functions $\Lambda_2(s)$ and $\Lambda_3(s)$, which are not limited to linear ones). The additional terms, $S_{1\alpha}^{(2)}$ and $S_{1\alpha}^{(3)}$, account explicitly for the continuous variation in cross-sectional dimensions via the coefficients Λ_2'/Λ_2 and Λ_3'/Λ_3. These additional terms, $S_{1\alpha}^{(2)}$ and $S_{1\alpha}^{(3)}$, produce a dependence of the shear stresses $S_{1\alpha}$ on the axial force F_1 and on the bending moments M_α that is absent in prismatic beams (Sokolnikoff, 1946; Love, 1944; Muskhelishvili, 1977) and cannot be predicted by resorting to results valid for the de Saint-Venant's cylinder.

In general, the solution to the current flexure problem (Eq. (15)) suggests that it is not possible to fully account for all the effects of taper and completely predict the shear stress distribution in a tapered cylinder by merely applying the formal solution valid for de Saint-Venant's cylinder, even when considering in this latter the actual axial variation of the cross-sectional parameters. The simple application of the de Saint-Venant's solution, allowing the cross-sectional parameters to vary, is equivalent to approximating the tapered cylinder with a stepped beam. This approximation can lead to inaccurate predictions of the shear stresses in the cross-sections of tapered cylinders, as will be shown ahead.

4. Application cases of the closed-form solution and analytical validation

This section applies the analytical solution derived in Section 3.1 to a tapered element (the variable-height beam depicted in Fig. 4(b)–(c)) previously studied in the literature through different approaches (Timoshenko and Goodier, 1951; Atkin, 1938; Bennati et al., 2016; Bertolini et al., 2019a; Migliaccio et al., 2022). This enables the validation of the analytical solution by comparisons with established formulas from the literature. Specifically, comparisons are made with the solution for the classical planar wedge (shown in Fig. 4(a)), as presented in foundational elasticity texts, such as Timoshenko and Goodier (1951), and with a solution based on the shear formula proposed in Migliaccio et al. (2022). A numerical validation with a benchmark FEM solution is presented in Section 5.

Fig. 4(a) illustrates a planar wedge of opening angle 2α, where a normal force N, a shear force T, and a bending moment M_O are applied at its vertex O.

Fig. 4(b)–(c) shows a variable-height beam and its rectangular cross-section. The beam's length is L, which is much greater than the dimensions of its cross-sections, implying that $\tan(\alpha) \simeq \alpha$. The cross-sectional dimensions are a constant thickness $2h_2$ and linearly variable height $2h_3$. The corresponding taper functions are $\Lambda_2 = 1$ and $\Lambda_3 = 1 - \alpha s/H_3$, where $2H_3$ is the height at the root section ($s = 0$).

The external actions on the beam are applied only at the end cross-sections and are statically equivalent to prescribed forces and moments. Those at the tip section ($s = L$) are represented in Fig. 4(b) and coincide with a normal force N along the beam's x-axis, a shear force T along the y-axis (parallel to the x_3-axis of the cross-section), and a bending moment M about the centroid of the cross-section relative to the x_2-axis. Forces and moments at the root section ($s = 0$), not represented in Fig. 4(b), are such that the global equilibrium of the beam is guaranteed.

The variable-height beam problem can be effectively addressed using the analytical solution derived in Section 3.1, which provides the complete *local* stress state S_{21} and S_{31} within the beam's cross-sections.

In the case of small thickness $2h_2$, the same problem can also be addressed by resorting to the solution of the theory of elasticity for the planar wedge (Timoshenko and Goodier, 1951). The shape of this latter is shown in Fig. 4(a), together with the axial force N, transverse force T, and bending moment $M_O = M + T(L_0 - L)$ applied at the vertex O. This solution methodology is illustrated in Section 4.2.

A third solution technique, commonly used for thin-walled beams, involves applying the new shear formula proposed in Migliaccio et al. (2022). It is noted that for the problem at hand such formula can be obtained by a direct application of the analytical solution derived in Section 3.1: indeed, the *local* stress state S_{21} and S_{31} can be integrated over the cross-sectional chord AB to determine the relevant *average* shear stress state. This solution is presented in Section 4.1.

4.1. Variable-height beam

The shear stresses in the cross-sections of the variable-height beam represented in Fig. 4(b)–(c) can be obtained by combining Eqs. (15)–(16), which yields

$$
S_{21} = -\frac{F_3}{J_2}\frac{2h_2^2\nu}{\pi^2(1+\nu)} f_2 + \frac{\Lambda_3'}{\Lambda_3}\frac{M_2}{J_2}\frac{6h_2^2\nu}{\pi^2(1+\nu)} f_2\,, \tag{18a}
$$

$$
\begin{aligned}
S_{31} = &-\frac{F_3}{J_2}\left(\frac{x_3^2 - h_3^2}{2} + \frac{\nu}{1+\nu}\frac{3x_2^2 - h_2^2}{6} - \frac{2h_2^2\nu}{\pi^2(1+\nu)} g_2\right) + \frac{\Lambda_3'}{\Lambda_3}\frac{F_1}{A} x_3\\
&+ \frac{\Lambda_3'}{\Lambda_3}\frac{M_2}{J_2}\left(\frac{3x_3^2 - h_3^2}{2} + \frac{\nu}{1+\nu}\frac{3x_2^2 - h_2^2}{2} + \frac{6h_2^2\nu}{\pi^2(1+\nu)} g_2\right),
\end{aligned}
\tag{18b}
$$

where the condition of constant thickness $2h_2$ has been enforced ($\Lambda_2 = 1$), together with $F_1 = N$, $F_3 = T$, and $M_2 = M + (s - L)T$.

For thin-walled beams, it is common practice to consider the average value of the shear stress state over the small thickness $2h_2$ or, in other words, over a chord AB parallel to the x_2-axis in Fig. 4(c). In the present case, the average value $\bar{S}_{21}$ of the stress field S_{21} over the chord AB is identically null, while the average value $\bar{S}_{31}$ of the stress field S_{31} turns out to be

$$
\bar{S}_{31} = -\frac{F_3}{J_2}\frac{x_3^2 - h_3^2}{2} + \frac{\Lambda_3'}{\Lambda_3}\left(\frac{F_1}{A} x_3 + \frac{M_2}{J_2}\frac{3x_2^2 - h_3^2}{2}\right). \tag{19}
$$

Eq. (19) exactly coincides with the average shear stress derivable by a direct application of the shear-flow formula proposed in Migliaccio et al. (2022), Migliaccio (2023a), and with the average shear stress in the thin-walled tapered I-beams considered in Balduzzi et al. (2017), Bertolini et al. (2019a).

It is important to note that, in the present work, Eq. (19) represents an *integral* information over the chord AB, obtained by utilizing the *local* knowledge of the complete shear stress state, S_{21} and S_{31}, as derived in Section 3.1 by analytically solving the PDE problem defined by Eqs. (8b), (8c), (9b).

It is also remarked that the first term in Eqs. (18a) and (18b) formally coincides with the solution of the classical theory of prismatic beams (Sokolnikoff, 1946; Love, 1944), except for the cross-sectional parameters, h_3, J_2, J_3, which are not constant here. Additionally, other terms are present in the current problem: they are proportional to coefficient Λ_3'/Λ_3 in Eqs. (18a)–(18b) and explicitly account for effects of taper that cannot be predicted by resorting to the classical theory of prismatic beams. The same can be said for Eq. (19), which has been derived by Eq. (18b).

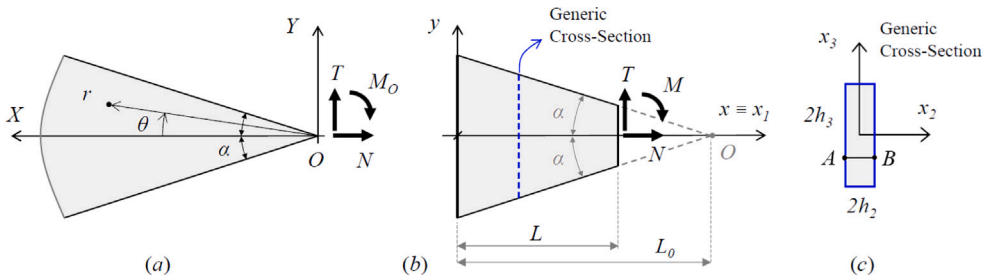

Fig. 4. Variable-height beam application case: (a) planar wedge of angle 2α, with normal force N, shear force T, and bending moment M_O applied at its vertex O; (b) variable-height beam acted upon by normal force N, shear force T, and bending moment M at the tip section; (c) generic cross-section of the variable-height beam, with indication of the cross-sectional dimension h_2, constant, and h_3, varying linearly along the beam's x-axis.

4.2. Wedge-like beam

The variable-height beam acted upon by external actions at the tip section statically equivalent to the normal force N, shear force T, and bending moment M, as shown in Fig. 4(b), resembles a portion of the infinite wedge represented in Fig. 4(a), subject to the same normal force N and shear force T at its vertex, plus a bending moment M_0. Under the condition that $M = M_0 - T(L_0 - L)$, the state of stress in the beam's cross-section can be recovered by resorting to the analytical solution of the theory of elasticity for the infinite wedge (Timoshenko and Goodier, 1951). Specifically, by this approach, it is possible to recover only the average value of the shear stress field S_{31} over the cross-sectional chord AB represented in Fig. 4(c).

Denoting with $\sigma_{r\theta}$, σ_{rr} and $\sigma_{\theta\theta}$ the stress fields in a two-dimensional wedge, expressed in polar coordinates r and θ with respect to the polar coordinate system $Or\theta$ illustrated in Fig. 4(a), the solution for the planar wedge under consideration, as reported in classical elasticity treatises (Timoshenko and Goodier, 1951), is given by:

$$\sigma_{r\theta} = \frac{M_O}{\sin(2\alpha) - 2\alpha\cos(2\alpha)} \frac{\cos(2\alpha) - \cos(2\theta)}{r^2}, \tag{20a}$$

$$\sigma_{rr} = \frac{2N}{\sin(2\alpha) + 2\alpha} \frac{\cos(\theta)}{r} + \frac{2T}{\sin(2\alpha) - 2\alpha} \frac{\sin(\theta)}{r} + \frac{M_O}{\sin(2\alpha) - 2\alpha\cos(2\alpha)} \frac{2\sin(2\theta)}{r^2}, \tag{20b}$$

with $\sigma_{\theta\theta} = 0$ identically.

From Eq. (20), it is straightforward to calculate the shear stress σ_{xy}, with respect to the Cartesian coordinate system, Oxy, represented in Fig. 4(b), as:

$$\sigma_{xy} = -\sigma_{rr}\sin(\theta)\cos(\theta) - \tau_{r\theta}\cos(2\theta), \tag{21}$$

where $r = \sqrt{X^2 + Y^2}$, $\cos(\theta) = X/r$, $\sin(\theta) = Y/r$, $Y = y$, and $X = L_0 - x$.

By combining Eqs. (20)–(21), the shear stress σ_{xy} at a point of the wedge of coordinates x, y can be explicitly expressed in terms of the normal force N, shear force T, and bending moment M_O. This produces a lengthy expression, which is difficult to interpret analytically. However, for small opening angle 2α of the wedge, a more compact engineering formula can be obtained. It reads:

$$\sigma_{xy} = -\frac{T}{I_w}\frac{y^2 - h_w^2}{2} + \frac{1}{h_w}\frac{dh_w}{dx}\left(\frac{N}{A_w}y + \frac{M - T(L-x)}{I_w}\frac{3y^2 - h_w^2}{2}\right), \tag{22}$$

where $h_w = (L_0 - x)\alpha$, $A_w = 2\alpha(L_0 - x)$, and $I_w = 2\alpha^3(L_0 - x)^3/3$.

The geometrical quantities A_w and I_w in Eq. (22) have been introduced to rewrite this latter in a form similar to Eq. (19), facilitating easier comparison. In particular, A_w and I_w represent the area and moment of inertia of a wedge's cross-section of height $2h_w$ and unit thickness. From this perspective, σ_{xy} turns out to be the average shear stress over the unit thickness and can be used to predict the average shear stress $\bar{S}_{31}$ over a cross-sectional chord AB of the variable-height beam represented in Fig. 4(b)–(c). Indeed, it is straightforward to verify that Eq. (22) exactly matches the expression for the average shear stress $\bar{S}_{31}$ derived in Section 4.1 (Eq. (19)), when considering that, in this case, $\Lambda_3(s) = 1 - \alpha s/H_3$. In other words, if the variable-height beam analysed in Section 4.1 is characterized by a linear variation of the cross-section height, it corresponds to the tapered wedge discussed in this section, and Eq. (19) coincides with the solution given in Eq. (22) for the tapered wedge.

It is concluded that the three analytical approaches, namely, the analytical solution derived in Section 3.1, the new shear formula proposed in Migliaccio et al. (2022), Migliaccio (2023a), and the method based on the classical solution for the infinite wedge (Timoshenko and Goodier, 1951), provide the same average shear stress state over the cross-sectional chords of the variable-height beam considered in this application example.

5. Numerical examples and comparisons with FEM results

This section illustrates results from numerical simulations conducted to corroborate the analytical findings of the present study. The analytical solutions derived for the bi-tapered beam in Section 3.1, the variable-height beam in Section 4.1, and the wedge-like beam in Section 4.2 have been implemented in a MATLAB code, utilizing the first ten terms of the series solution in Eq. (17). The results obtained have been compared with benchmark numerical solutions obtained in ANSYS using the Finite Element Method (FEM), with a fine mesh of structural solid elements.

The shear stress distributions in two different cantilever tapered beams, shaped to resemble structural elements such as shear webs of large horizontal axis wind turbine blades (Migliaccio et al., 2022; Migliaccio, 2023a), subject to a transverse external force at the free end, are analysed: in the first test case (Section 5.1), the beam has a variable height and constant thickness (variable-height beam); in the second (Section 5.2), both cross-sectional dimensions vary along the beam's axis (bi-tapered beam).

Specifically, in Section 5.1, the analytical solution derived for the variable-height beam (Section 4.1), resembling a portion of an infinite wedge (Timoshenko and Goodier, 1951), is compared with the wedge-based solution given by Eq. (22), with the shear formula proposed in Migliaccio et al. (2022), with the solution obtained using a stepped-beam approach, and with the benchmark numerical solution provided by ANSYS.

For the bi-tapered beam, which (unlike the variable-height beam) does not resemble a portion of a planar wedge, the accuracy of the analytical solution derived in Section 3.1 can only be verified by comparison with the benchmark FEM solution. This is done in Section 5.2, where comparisons with the shear formula (Migliaccio et al., 2022) and with the outcomes of a stepped-beam approach are also reported.

5.1. Variable-height beam

A variable-height beam is considered again, with an axial length $L = 100$ m and a constant cross-sectional thickness, $2h_2 = constant$.

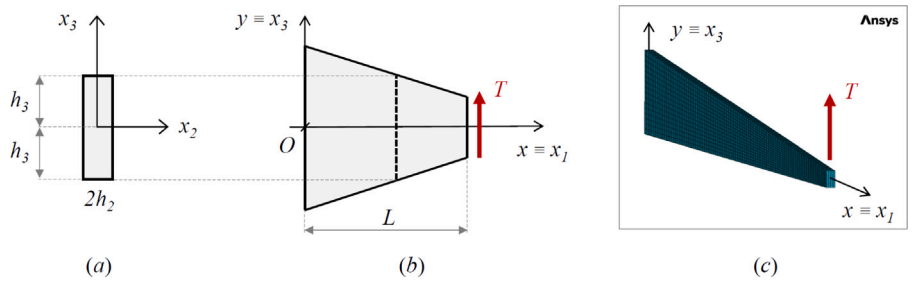

Fig. 5. Variable-height beam: (a) cross-sectional view, with indication of the constant thickness $2h_2$ and variable height $2h_3$; (b) lateral view, with the transverse external force T applied at the tip section; (c) three-dimensional view of the FEM model in the ANSYS environment.

The cross-sectional height, $2h_3$, at the root section ($s = 0$) is 5 m and decreases linearly towards the tip section ($s = L$) to 50% of the root height. Accordingly, the taper functions are $\Lambda_2 = 1$ (for constant thickness) and $\Lambda_3 = 1 - 0.5\, s/L$, with $s/L \in [0, 1]$. The beam's material properties are defined by a Young's modulus $Y = 70$ GPa and a Poisson's ratio $\nu = 0.25$. The beam is fixed at the root section, while external loads are applied at the tip section and are statically equivalent to a prescribed transverse force T, as illustrated in Fig. 5.

Various approaches are used to determine the shear stress distributions in the cross-sections of this variable-height beam. These approaches are briefly referred to here as TAP (shorthand for *Tapered*), WED (*Wedge*), SFF (*Shear-Flow Formula*), STP (*Stepped*), and FEM (*Finite Element Method*). The corresponding solutions are, respectively: the closed-form solution derived in Section 3.1 (for bi-tapered beams) and in Section 4.1 (for variable-height beams); the wedge-based (Timoshenko and Goodier, 1951) analytical solution provided by Eq. (22); the analytical solution based on the shear formula proposed in Migliaccio et al. (2022); the solution obtained using a stepped-beam approach; and, finally, the benchmark numerical solution provided by ANSYS, based on a fine mesh of structural solid elements, such as the tree-dimensional *element type* 185 (Madenci and Guven, 2015). The outcomes of these approaches are compared in Figs. 6 and 7.

Specifically, Fig. 6 shows the shear stress distributions, S_{31}, in a variable-height beam with thickness $2h_2 = 0.5$ m, at five reference cross-sections whose distance from the root section is, respectively, 10%, 30%, 50%, 70%, and 90% of the beam's length L: the blue lines, labelled TAP, denote stress distributions based on the analytical solution (18), which explicitly accounts for the effect of taper through coefficient Λ_3'/Λ_3; yellow lines, labelled WED, are based on the infinite wedge (Timoshenko and Goodier, 1951), whose analytical solution has been exploited to obtain Eq. (22); green lines (label SFF) are obtained using the shear formula proposed in Migliaccio et al. (2022), which coincides with Eq. (19) for the current beam's shape; black lines (label STP) are the results of a stepped-beam approach; finally, red marks represent the benchmark FEM solution.

Fig. 7 replicates the results of Fig. 6 for an increased cross-sectional thickness, specifically $2h_2 = 4.0$ m. Accordingly, this variable-height beam is characterized by a thickness-to-height h_2/h_3 varying from 0.8 at the root section to 0.4 at the tip section, which is eight times larger than the case in Fig. 6 (where $2h_2 = 0.5$ m).

It is noted that the shear stress distributions based on the WED and SFF approaches depend solely on the cross-sectional variable x_3 and are independent of the cross-sectional variable x_2, as per Eqs. (22) and (19), respectively. These approaches cannot provide more accurate results. On the contrary, the analytical approaches TAP and STP, as well as the FEM solution, can account for the dependence of the shear stress distributions on both variables, x_2 and x_3. This is evident in Fig. 7, where the thickness-to-height h_2/h_3 ratio of the beam's cross-sections is significantly larger than in Fig. 6. Shear stress variation through the thickness is generally negligible in thin-walled beams, as it is confirmed from the results presented in Fig. 6. When the thickness-to-height ratio h_2/h_3 is not sufficiently small, stress predictions using the WED and SFF approaches may yield inaccurate results (see, for example, Fig. 7).

Furthermore, it is important to emphasize that the stepped-beam approach (STP) does not yield accurate stress predictions, either quantitatively or qualitatively, as evidenced by the black lines in Figs. 6 and 7 when compared to the FEM solution (red marks), regardless of the thickness-to-height h_2/h_3 ratio of the beam.

In general, the only lines closely matching the FEM red marks in all cases are the blue ones (labelled TAP in Figs. 6 and 7), corresponding to the analytical solution derived in the present study and reported in Section 4.1.

5.2. Bi-tapered beam

A bi-tapered beam is considered here, with a length $L = 100$ m. The cross-sectional dimensions, h_2 and h_3, at the root section ($s = 0$) are 1.5 m and 2.5 m, respectively. These dimensions decrease linearly towards the tip section ($s = L$), reaching 50% and 30% of their root values. Accordingly, the taper functions are $\Lambda_2 = 1 - 0.5\, s/L$ and $\Lambda_3 = 1 - 0.7\, s/L$, with $s/L \in [0, 1]$. The material properties are defined by a Young's modulus $Y = 70$ GPa and a Poisson's ratio $\nu = 0.25$. The loading condition mirrors the previous test case: the root section is fixed, while the tip section is acted upon by external loads statically equivalent to a prescribed transverse force T.

Fig. 8 illustrates the shear stress distributions S_{31} at five reference cross-sections located at 10%, 30%, 50%, 70%, and 90% of the beam's length L: the blue lines, labelled TAP, are derived from the analytical solution presented in Section 3.1, which accounts for the effect of taper through coefficients Λ_2'/Λ_2 and Λ_3'/Λ_3 in Eqs. (15)–(16); green-lines, labelled SFF, are based on the shear formula proposed in Migliaccio et al. (2022); black lines are obtained using a stepped-beam approach (label STP); finally, red marks represent the benchmark FEM solution provided by ANSYS.

The stress field S_{31} predicted using the shear formula (SFF) is independent of the cross-sectional variable x_2 and depends solely on x_3. On the contrary, the analytical solution derived in Section 3.1, labelled TAP, properly accounts for the dependence of the stress field S_{31} on both variables, x_2 and x_3, as is confirmed by comparisons with the FEM solution (red marks). In particular, it is observed that also the symmetry of function $S_{31}(x_2, x_3)$ with respect to the cross-sectional axes is accurately predicted: Fig. 8 illustrates, for example, the stress distributions $S_{31}(x_2 = -0.1h_2, x_3) \equiv S_{31}(x_2 = +0.1h_2, x_3)$ and $S_{31}(x_2 = -0.9h_2, x_3) \equiv S_{31}(x_2 = +0.9h_2, x_3)$.

In addition, it is noted, once again, the inadequacy of the stepped-beam approach (black lines, labelled STP) in predicting (either quantitatively or qualitatively) the shear stresses in a tapered beam. The only lines closely matching the benchmark FEM solution (red marks) in all cases are the blue ones (labelled TAP), corresponding to the analytical solution derived in Section 3.1.

For completeness, Fig. 9 illustrates also the distribution of the stress field S_{21} across the same cross-sections, located at 10%, 30%, 50%, 70%, and 90% of the beam's length L. The legend of colours and labels remains the same as in Fig. 8 and is therefore omitted. In its place, a

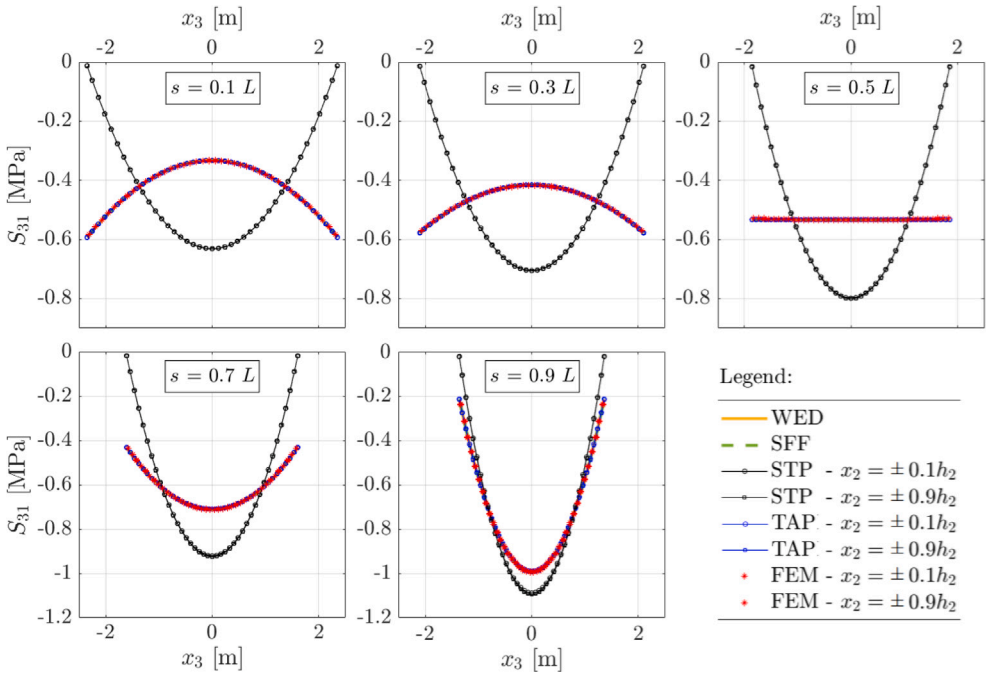

Fig. 6. Shear stress distributions S_{31} at different cross-sections of a variable-height beam with constant thickness $2h_2 = 0.5$ m, for $T = -1000$ kN, as predicted using different approaches: FEM (red marks), TAP (blue lines), STP (black lines), WED (yellow lines), and SFF (green lines).

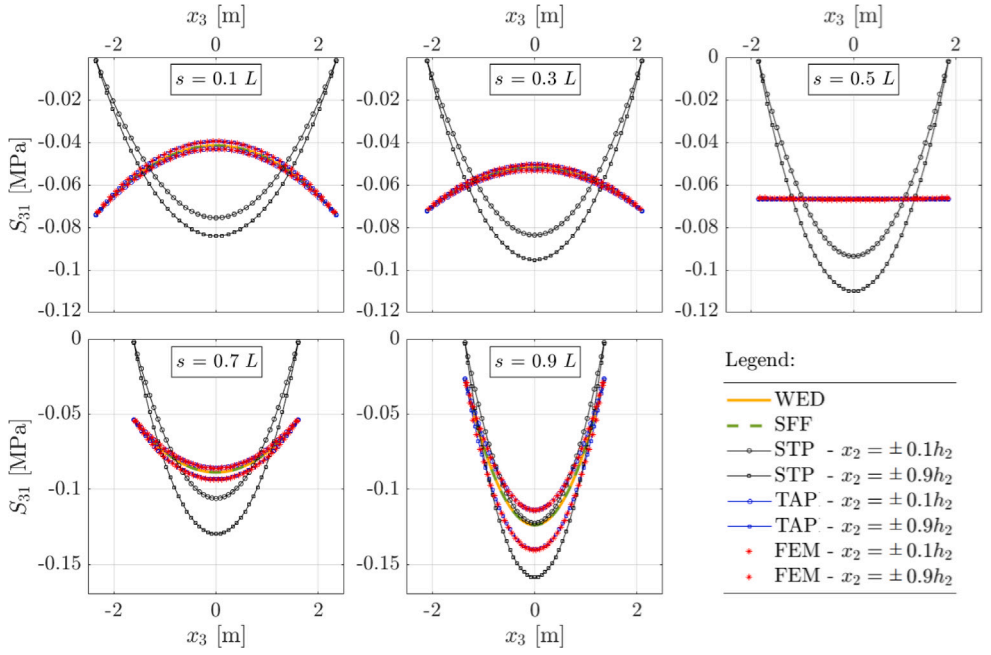

Fig. 7. Shear stress distributions S_{31} at different cross-sections of a variable-height beam with constant thickness $2h_2 = 4.0$ m, for $T = -1000$ kN, as predicted using different approaches: FEM (red marks), TAP (blue lines), STP (black lines), WED (yellow lines), and SFF (green lines).

close-up view of the shear stress distribution S_{21} is provided for the cross-section located at $s = 0.9L$. This view highlights more clearly the following important points: (i) predictions from the shear formula (blue lines, SFF) show no dependence on x_2 and remain identically zero across all cross-sections; (ii) predictions from the stepped-beam approach (black lines, STP) are inadequate, both quantitatively and qualitatively; (iii) the only lines closely matching the FEM solution (red marks) across all cases are the blue lines labelled TAP.

Other numerical analyses have been conducted, exploring various geometries and loading conditions. Further examples will also be provided in a forthcoming paper, where the stress and strain state of other tapered elements used in structural engineering applications will be examined using the method and solutions presented in this study. The general conclusion here is that the new analytical expressions for the shear stresses derived in this study, as solutions to the PDEs (8b)–(8c) with boundary condition (9b), show excellent agreement with the benchmark FEM solution. In contrast, the inadequacy of a stepped-beam modelling approach in predicting shear stresses in tapered elements is proved, as it could be expected from examining the new analytical solution presented in Section 3.1.

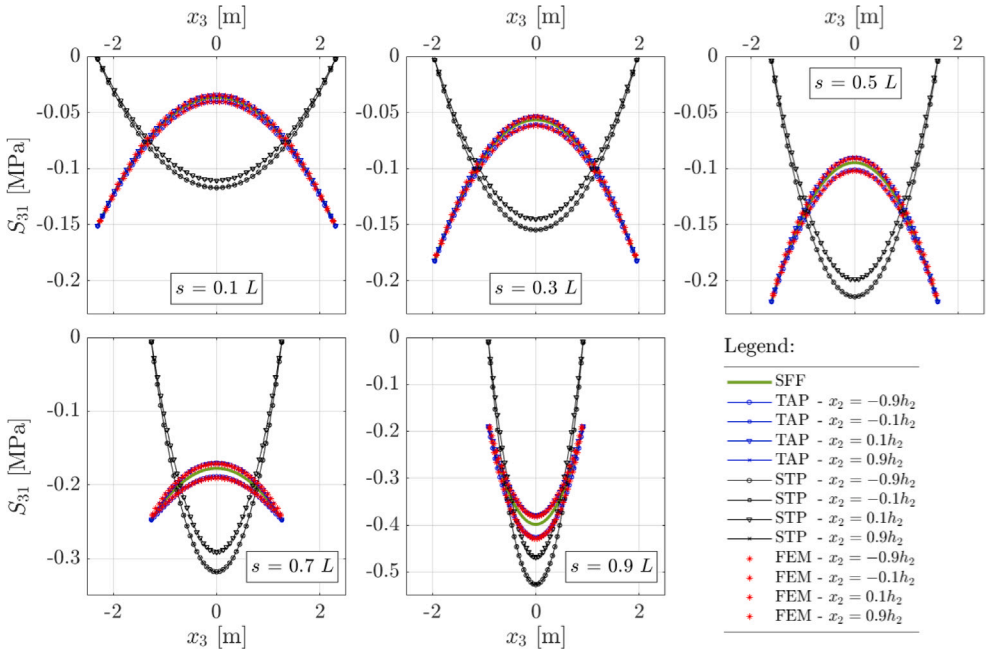

Fig. 8. Shear stress distributions S_{31} at different cross-sections of a bi-tapered beam subject to a tip load $T = -1000$ kN, as predicted using different approaches: FEM (red marks), TAP (blue lines), STP (black lines), and SFF (green lines).

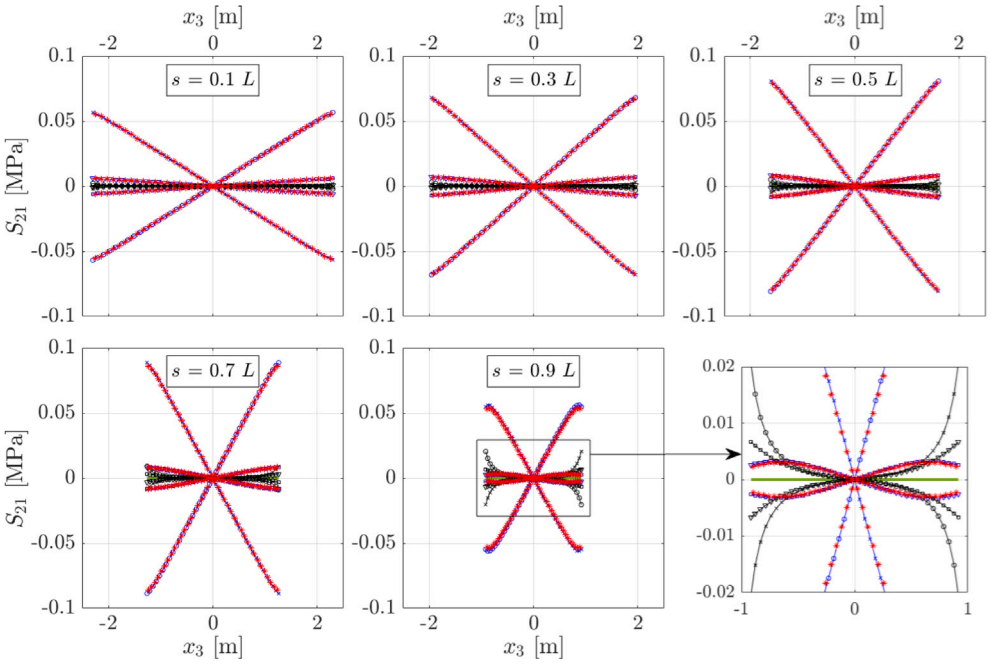

Fig. 9. Shear stress distributions S_{21} at different cross-sections of a bi-tapered beam, for a tip force $T = -1000$ kN, as predicted using different approaches: FEM (red marks), TAP (blue lines), STP (black lines), and SFF (green lines). For more clarity, it is also presented a close-up view of the distribution over the cross-section $s = 0.9L$, to the right of this latter.

6. Conclusions and perspectives

The influence of taper on the stress fields in slender elastic cylinders with a straight axis and tapered cross-sections has been examined in this work. Compared to the well-known de Saint-Venant's cylinder, where cross-sectional dimensions are constant, the continuous variation in cross-sectional dimensions along the axis of a tapered cylinder generates additional shear stress distributions within its cross-sections. These additional distributions are not trivial, self balanced over the cross-section, and differ substantially from those predicted by stepped-beam approaches. This has been demonstrated analytically in the paper and validated through comparisons with benchmark FEM solutions obtained in ANSYS, using a fine mesh of solid elements.

The analytical investigation in the paper relies on a physical-mathematical model for non-prismatic slender cylinders presented in recent works, where a variational principle establishes partial differential equations (PDEs) and boundary conditions that govern the stress state in such elements. In the present work, such PDEs have been revisited and a new analytical solution has been obtained for rectangular cross-sectioned tapered cylinders, subject to external loads applied solely at the end cross-sections. The resulting expressions obtained for the cross-sectional stresses and strains have been shown to extend

those valid for the de Saint-Venant's cylinder, reducing exactly to these latter only in the prismatic case. Furthermore, the new analytical solution derived in this study has highlighted the limitations of stepped-beam modelling approaches for stress predictions in tapered slender solids, underscoring their inadequacy in capturing the stress variations introduced by taper.

In general, it has been found that the cross-sectional shear stresses in tapered cylinders can be expressed as the sum of a first contribution resembling the solution for the de Saint-Venant's cylinder (with the distinction that cross-sectional dimensions are variable in tapered cylinders), plus additional terms proportional to the derivative of the taper coefficients, Λ_2' and Λ_3'. These additional terms have been shown to produce a dependence of the shear stresses on the axial force and on the bending moments that is absent in prismatic beams and that depends explicitly on the continuous variation in the cross-sectional dimensions. Specifically, the obtained solution has suggested that it is not possible to fully account for all the effects of taper and completely predict the shear stress distribution in a tapered cylinder by merely applying the formal solution valid for de Saint-Venant's cylinder, even when considering in this latter the actual variation of the cross-sectional parameters. The simple application of the de Saint-Venant's solution, allowing the cross-sectional parameters to vary, which is equivalent to approximate the tapered cylinder with a stepped beam, has been shown to lead to inaccurate stress predictions in tapered cylinders, as also confirmed by FEM analyses.

Two validation examples have been presented: one for a variable-height beam and another for a bi-tapered beam. The analytical solution derived for the variable-height beam has been compared both analytically and numerically with the classical elasticity solution for a planar wedge (Timoshenko and Goodier, 1951), with a solution based on the shear formula proposed in Migliaccio et al. (2022), and with the results from a stepped-beam modelling approach. The shear stress distributions obtained using these approaches have finally been validated by comparison with the benchmark FEM solution provided by ANSYS. The findings of the analysis indicate that the new analytical solution derived in Section 4.1 is the only one that consistently matches the FEM solution across all cases, irrespective of the beam's thickness. For thin-walled elements (namely, small thickness-to-height ratio of the cross-sections), the wedge-based solution and shear formula have been shown to yield satisfactory results. In contrast, the stepped-beam approach has been demonstrated to fail in providing accurate stress predictions, both quantitatively and qualitatively, regardless of the cross-section thickness-to-height ratio. A similar analysis has been performed for a bi-tapered beam, where the analytical solution presented in Section 3.1 has been evaluated alongside the shear formula and the stepped-beam approach. Validation against the FEM solution has confirmed the stepped-beam approach's inadequacy in predicting shear stresses in tapered beams.

Additional numerical examples, load cases, and technical applications of the analytical results from this study could be explored. For instance, the inertial loads generated by blade rotation are especially significant in helicopter rotor blades due to their high rotational speeds and should be accounted for when predicting their stress and strain state. This application, along with other potential technical uses of the analytical solution derived in the present study, will be explored in a forthcoming work.

Beyond taper effects, future efforts will also focus on investigating the influence of additional geometric parameters, such as the initial curvature of the beam's axis and the initial twist of tapered cross-sections (Migliaccio and Ruta, 2021). Other areas of interest include the analytical study of the influence of key material parameters, such as those describing the anisotropic behaviour of classical materials like timber, which are commonly used in sustainable structural applications (Sciomenta et al., 2024, 2020), as well as the mechanical properties of metamaterials (Barchiesi et al., 2019; Turco et al., 2020), which are gaining increasing attention for innovative applications. Future developments could also explore the linear and nonlinear dynamic behaviour of tapered cylinders under external excitations, dead loads and follower forces (similar to the analysis conducted in Luongo and D'Annibale (2012), Migliaccio and D'Annibale (2024) for prismatic cases), as well as the effects of damping devices (of the type considered in Luongo and D'Annibale (2014, 2017), e.g.) on the stability of cylinders with tapered cross-sections. Additionally, the influence of piezoelectric patches on tapered elements for vibration control and energy harvesting (as is done in D'Annibale et al. (2016), Casalotti and D'Annibale (2021, 2022b,a) for prismatic elements) also represents an intriguing area for future investigations.

CRediT authorship contribution statement

Giovanni Migliaccio: Writing – review & editing, Methodology, Formal analysis, Conceptualization. **Francesco D'Annibale:** Writing – review & editing, Supervision, Methodology.

Funding

This research did not receive any specific grant from funding agencies in the public, commercial, or not-for-profit sectors.

Declaration of competing interest

The authors declare that they have no known competing financial interests or personal relationships that could have appeared to influence the work reported in this paper.

Appendix. Shear stresses in the torsion problem

For completeness, it is reported in this section the solution of the partial differential equation (8a) with boundary condition (9a), which is formally identical to the mathematical problem that provides the de Saint-Venant's out-of-plane warping function associated with the torsion problem (Sokolnikoff, 1946). Accordingly, for a rectangular cross-sectioned tapered cylinder, the scalar field ω can be expressed in the form

$$\omega = \frac{M_1}{GJ_1}\left[x_2x_3 - \frac{32h_2^3}{\pi^3}\sum_{n=0}^{\infty}\frac{(-1)^n}{(2n+1)^3}\frac{\sinh\left(c_nx_3\right)}{\cosh\left(c_nh_3\right)}\sin\left(c_nx_2\right)\right], \tag{A.1}$$

where $c_n = (n+1/2)\pi/h_2$ and $M_1 = GJ_1k_1$ is the torsional moment, which is proportional to the torsional curvature k_1 through the material shear modulus G and the torsional moment of inertia J_1. For the problem at hand, this latter is

$$J_1 = \frac{8h_3h_2^3}{3} - \frac{1024h_2^4}{\pi^5}\sum_{n=0}^{\infty}\frac{\tanh\left(\frac{(2n+1)\pi h_3}{2h_2}\right)}{(2n+1)^5}. \tag{A.2}$$

Given the scalar field ω, the corresponding shear stresses are

$$S_{21} = -\frac{M_1}{GJ_1}\frac{16h_2^2}{\pi^3}\sum_{n=0}^{\infty}\frac{(-1)^n}{(2n+1)^2}\frac{\sinh\left(c_nx_3\right)}{\cosh\left(c_nh_3\right)}\cos\left(c_nx_2\right), \tag{A.3a}$$

$$S_{31} = \frac{M_1}{GJ_1}\left[2x_2 - \frac{16h_2^2}{\pi^2}\sum_{n=0}^{\infty}\frac{(-1)^n}{(2n+1)^2}\frac{\cosh\left(c_nx_3\right)}{\cosh\left(c_nh_3\right)}\sin\left(c_nx_2\right)\right]. \tag{A.3b}$$

Eq. (A.3) show that the solution to the torsion problem for the rectangular cross-sectioned tapered cylinder under study is formally identical to the solution for the de Saint-Venant's cylinder with the same cross-sectional shape, except for the fact that the cross-sectional parameters (h_2, h_3, J_1) are not constant here, but vary along the cylinder's axis according to prescribed taper functions, $\Lambda_2(s)$, $\Lambda_3(s)$.

The solution to the current torsion problem indicates that it is possible to account for the effects of taper and predict the shear stress

distribution in this tapered cylinder under pure torsion by merely applying the formal solution valid for the de Saint-Venant's cylinder, considering in this latter the actual variation of the cross-sectional parameters along the cylinder's axis. Unlike the flexure problem (addressed in Section 3.1), there are no additional shear stress distributions (such as those proportional to coefficients Λ_2' and Λ_3' in Eq. (15a)) that need to be considered.

Data availability

The data that support the findings of this study are available within the paper.

References

Atkin, E., 1938. Tapered beams: Suggested solutions for some typical aircraft cases. Aircr. Eng. Aerosp. Technol. 10 (11), 347–351.

Balduzzi, G., Aminbaghai, M., Sacco, E., Fussl, J., Eberhardsteiner, J., Auricchio, F., 2016. Non-prismatic beams: A simple and effective timoshenko-like model. Int. J. Solid Struct. 90, 236–250.

Balduzzi, G., Hochreiner, G., Füssl, J., 2017. Stress recovery from one dimensional models for tapered bi-symmetric thin-walled I beams: deficiencies in modern engineering tools and procedures. Thin-Walled Struct. 119, 934–945.

Barchiesi, E., Spagnuolo, M., Placidi, L., 2019. Mechanical metamaterials: a state of the art. Math. Mech. Solids 24 (1), 212–234.

Bennati, S., Bertolini, P., Taglialegne, L., Valvo, P., 2016. On shear stresses in tapered beams. In: 21st Italian Conference on Computational Mechanics and 8th Meeting of the AIMETA Materials Group. 27–29 June, Lucca, Italy.

Bertolini, P., Eder, M., Taglialegne, L., Valvo, P., 2019a. Stresses in constant tapered beams with thin-walled rectangular and circular cross sections. Thin-Walled Struct. 137, 527–540.

Bertolini, P., Sarhadi, A., Stolpe, M., Eder, M., 2019b. Comparison of stress distributions between numerical cross-section analysis and 3D analysis of tapered beams. In: 22nd International Conference on Composite Materials. 11–16 August, Melbourne, Australia.

Bertolini, P., Taglialegne, L., 2020. Analytical solution of the stresses in doubly tapered box girders. Eur. J. Mech. A Solids 81, 103969.

Bleich, F., 1932. Stahlhochbauten Bd. 1. Springer, Berlin.

Casalotti, A., D'Annibale, F., 2021. Improving the linear stability of the visco-elastic Beck's beam via piezoelectric controllers. J. Appl. Comput. Mech. 7, 1098–1109.

Casalotti, A., D'Annibale, F., 2022a. On the effects of a beam-like piezoelectric passive controller on the linear stability of the visco-elastic Beck's beam. Mech. Res. Commun. 125, 103980.

Casalotti, A., D'Annibale, F., 2022b. A rod-like piezoelectric controller for the improvement of the visco-elastic Beck's beam linear stability. Struct. Control Health Monit. 29 (2), 2865.

Chockalingam, N., Nithyadharan, M., Pandurangan, V., 2020. Shear stress distribution in tapered I-beams: Analytical expression and finite element validation. Thin-Walled Struct. 157, 107152.

D'Annibale, F., Rosi, G., Luongo, A., 2016. Piezoelectric control of hopf bifurcations: A non-linear discrete case study. Int. J. Non-Linear Mech. 80, 160–169.

Dell'Isola, F., Bichara, A., 2005. Elementi di algebra tensoriale con applicazioni alla meccanica dei solidi. Società Editrice Esculapio, Bologna.

dell'Isola, F., Eugster, S., Fedele, R., Seppecher, P., 2022. Second-gradient continua: From Lagrangian to Eulerian and back. Math. Mech. Solids 27 (12), 2715–2750.

DesRoches, R., Migliaccio, G., Royer-Carfagni, G., 2022. Structures that can be made with carbon nanotube fibers but not with other materials. J. Eng. Mech. 148 (12), 04022077.

Galilei, G., 1638. Discorsi e dimostrazioni matematiche intorno a due nuove scienze attenenti alla mecanica e i movimenti locali. Ludovico Elzeviro, Netherlands, Leiden.

Galilei, G., 1954. Two New Sciences. Dover, New York, Translated by H. Crew and A. de Salvio.

Griffith, D., Ashwill, T., Resor, B., 2012. Large offshore rotor development: design and analysis of the Sandia 100-meter wind turbine blade. In: Proc. of the 53rd Structures, Structural Dynamics and Materials Conference, 23–26 April.

Gurtin, M., 1981. An Introduction to Continuum Mechanics, Mathematics in Science and Engineering. Academic Press, Pittsburgh.

Hodges, D., Ho, J., Yu, W., 2008. The effect of taper on section constants for in-plane deformation of an istotropic strip. J. Mech. Mater. Struct. 3, 425–440.

Hodges, D., Rajagopal, A., Ho, J., Yu, W., 2010. Stress and strain recovery for the in-plane deformation of an isotropic tapered strip-beam. J. Mech. Mater. Struct. 5, 963–975.

Jourawski, D., 1856. Sur la résistance d'un corps prismatique et d'une piéce composée en bois ou on tôle de fer à une force perpendiculaire à leur longeur. Ann. Des Ponts Chaussées 12, 328–351.

Krahula, J., 1975. Shear formula for beams of variable cross section. AIAA J. 13 (10), 1390–1391.

Love, A., 1944. A Treatise on the Mathematical Theory of Elasticity. Dover Publications, New York.

Luongo, A., D'Annibale, F., 2012. Bifurcation analysis of damped visco-elastic planar beams under simultaneous gravitational and follower forces. J. Mod. Phys. B 26, 1246015.

Luongo, A., D'Annibale, F., 2014. On the destabilizing effect of damping on discrete and continuous circulatory systems. J. Sound Vib. 133, 6723–6741.

Luongo, A., D'Annibale, F., 2017. Nonlinear hysteretic damping effects on the post-critical behaviour of the visco-elastic Beck's beam. Math. Mech. Solids 22 (6), 1347–1365.

Madenci, E., Guven, I., 2015. The Finite Element Method and Applications in Engineering Using Ansys. Springer, New York, USA.

Mercuri, V., Balduzzi, G., Asprone, D., Auricchio, F., 2020. Structural analysis of non-prismatic beams: Critical issues, accurate stress recovery, and analytical definition of the finite element (FE) stiffness matrix. Eng. Struct. 213, 110252.

Migliaccio, G., 2022a. Analytical determination of the influence of geometric and material design parameters on the stress and strain fields in non-prismatic components of wind turbines. J. Phys. Conf. Ser. 2265 (032033).

Migliaccio, G., 2022b. Analytical evaluation of stresses and strains in inhomogeneous non-prismatic beams undergoing large deflections. Acta Mech. 233, 2815–2827.

Migliaccio, G., 2023a. Analytical prediction of the cross-sectional shear flow in non-prismatic inhomogeneous beamlike solids. Thin-Walled Struct. 183, 110384.

Migliaccio, G., 2023b. Analytical solutions of partial differential equations modeling the mechanical behavior of non-prismatic slender continua. Mathematics 11(23) (4723).

Migliaccio, G., D'Annibale, F., 2024. On the role of different nonlinear damping forms in the dynamic behavior of the generalized Beck's column. Nonlinear Dynam. 112, 13733–13750.

Migliaccio, G., Ruta, G., 2020. Rotor blades as curved, twisted, and tapered beam-like structures subjected to large deflections. Eng. Struct. 222, 111089.

Migliaccio, G., Ruta, G., 2021. The influence of an initial twisting on tapered beams undergoing large displacements. Meccanica 56 (7), 1831–1845.

Migliaccio, G., Ruta, G., Barsotti, R., Bennati, S., 2022. A new shear formula for tapered beamlike solids undergoing large displacements. Meccanica 57, 1713–1734.

Migliaccio, G., Ruta, G., Bennati, S., Barsotti, R., 2020. Beamlike models for the analyses of curved, twisted and tapered horizontal-axis wind turbine (HAWT) blades undergoing large displacements. Wind Energy Sci. 5, 685–698.

Muskhelishvili, N., 1977. Some Basic Problems of the Mathematical Theory of Elasticity. Springer, Dordrecht.

Navier, C., 1864. Résumé des leçons données à l'école des ponts et chaussées sur l'application de la mécanique a l'établissement des constructions et des machines, 3me éd. avec des notes étendues par M Barré de Saint-Venant. Dunod, Paris.

Paglietti, A., Carta, G., 2009. Remarks on the current theory of shear strength of variable depth beams. Open Civ. Eng. J. 3, 28–33.

Patni, M., Minera, S., Weaver, P., Pirrera, A., 2020. Efficient modelling of beam-like structures with general non-prismatic, curved geometry. Comput. Struct. 240, 106339.

Pugsley, A., Weatherhead, R., 1942. The shear stresses in tapered beams. Aeronaut. J. 46 (381), 218–226.

Rubin, M., 2000. Cosserat theories: shells, rods and points. Solid Mechanics and Its Applications, vol. 79, Kluwer Academic Publishers, The Netherlands.

Ruta, G., Pignataro, M., Rizzi, N., 2006. A direct one-dimensional beam model for the flexural-torsional buckling of thin-walled beams. J. Mech. Mater. Struct. 1, 1479–1496.

Saksena, G., 1944. Shear stress in a tapering beam. Aircr. Eng. Aerosp. Technol. 16 (2), 47–50.

Sarhadi, A., Eder, M., 2024. 3D numerical cross-section analysis of a tapered beam slice. Iran. J. Sci. Technol. Trans. Mech. Eng. 48, 1659–1676.

Sciomenta, M., Paoletti, A., Stamopoulos, A., 2024. Experimental investigation of the mode I fracture toughness behaviour of timber adhesive joints: The synergistic effect of the adhesive type and the bondline thickness. Int. J. Adhes. Adhes. 130, 103652.

Sciomenta, M., Rinaldi, V., Bedon, C., Fragiacomo, M., 2020. Application of modal-displacement based design method to multi-story timber blockhaus structures. Appl. Sci. 10, 3889.

Shin, D., Choi, S., Jang, G., Kim, Y., 2016. Finite element beam analysis of tapered thin-walled box beams. Thin-Walled Struct. 102, 205–214.

Slocum, S., 1911. A general formula for the shearing deflection of arbitrary cross-section, either variable or constant. J. Franklin Inst. 171 (4), 365–389.

Sokolnikoff, I., 1946. Mathematical Theory of Elasticity. McGraw-Hill Inc., New York.

Su, X., Zhou, M., 2022. Analysis of shear stresses in tapered beams under bending, shear and axial force. Structures 41, 849–865.

Timoshenko, S., Goodier, J., 1951. Theory of Elasticity. McGraw-Hill, New York.

Trahair, N., Ansourian, P., 2016. In-plane behaviour of web-tapered beams. Eng. Struct. 108, 47–52.

Turco, E., Barchiesi, E., Giorgio, I., dell'Isola, F., 2020. A Lagrangian Hencky-type non-linear model suitable for metamaterials design of shearable and extensible slender deformable bodies alternative to timoshenko theory. Int. J. Non-Linear Mech. 123, 103481.

Vilar, M., Hadjiloizi, D., Masjedi, P., Weaver, P., 2021. Stress analysis of generally asymmetric non-prismatic beams subject to arbitrary loads. Eur. J. Mech. A Solids 90, 104284.
Vo, D., Li, X., Nanakorn, P., Bui, T., 2021. An efficient isogeometric beam formulation for analysis of 2D non-prismatic beams. Eur. J. Mech. A Solids 89, 104280.
Xu, Y., Zhou, D., 2009. Elasticity solution of multi-span beams with variable thickness under static loads. Appl. Math. Model. 33, 2951–2966.
Zappino, E., Viglietti, A., Carrera, E., 2018. Analysis of tapered composite structures using a refined beam theory. Compos. Struct. 183, 42–52.